SCIENTIFIC REPORTS

OPEN

Strain-balanced type-II superlattices for efficient multi-junction solar cells

Received: 16 January 2017
Accepted: 15 May 2017
Published online: 21 June 2017

A. Gonzalo[1], A. D. Utrilla[1], D. F. Reyes[2], V. Braza[2], J. M. Llorens[3], D. Fuertes Marrón[4], B. Alén[3], T. Ben[2], D. González[2], A. Guzman[1], A. Hierro[1] & J. M. Ulloa[1]

Multi-junction solar cells made by assembling semiconductor materials with different bandgap energies have hold the record conversion efficiencies for many years and are currently approaching 50%. Theoretical efficiency limits make use of optimum designs with the right lattice constant-bandgap energy combination, which requires a 1.0–1.15 eV material lattice-matched to GaAs/Ge. Nevertheless, the lack of suitable semiconductor materials is hindering the achievement of the predicted efficiencies, since the only candidates were up to now complex quaternary and quinary alloys with inherent epitaxial growth problems that degrade carrier dynamics. Here we show how the use of strain-balanced GaAsSb/GaAsN superlattices might solve this problem. We demonstrate that the spatial separation of Sb and N atoms avoids the ubiquitous growth problems and improves crystal quality. Moreover, these new structures allow for additional control of the effective bandgap through the period thickness and provide a type-II band alignment with long carrier lifetimes. All this leads to a strong enhancement of the external quantum efficiency under photovoltaic conditions with respect to bulk layers of equivalent thickness. Our results show that GaAsSb/GaAsN superlattices with short periods are the ideal (pseudo) material to be integrated in new GaAs/Ge-based multi-junction solar cells that could approach the theoretical efficiency limit.

In the solar cell community, there is a quest for surpassing the 50% efficiency psychological barrier, which implies that half of the light energy coming from the Sun would be transformed into electric power. The solar cell efficiency tables[1] show how close we are to reach that limit: 46.0% under concentration and 38.8% under AM1.5 G conditions. Theoretical efficiency limits make use of optimum multi-junction designs with the ideal lattice constant-bandgap energy combination but, sometimes, lack of suitable, easy to control semiconductor materials hinders their implementation. For instance, in the standard (Al)InGaP/(In)GaAs/Ge solar cell structure, the addition of a lattice-matched sub-cell tuned to the 1.0–1.15 eV spectral range provides such an optimum multi-layer design[2,3]. Under standard AM1.5 G conditions, detailed-balance calculations predict 44.4% efficiency for a 3-junction AlInGaP(1.9 eV)/GaAs(1.4 eV)/1.0 eV solar cell and 47.7% for a 4-junction AlInGaP(1.9 eV)/GaAs(1.4 eV)/1.0 eV/Ge(0.66 eV) solar cell. Both designs would easily leave behind the 50% limit when operated under concentration[4]. After the two consecutive world efficiency records set by Solar Junction CA[5], which were preceded by strong efforts in optimizing single-junction cells[6], GaInNAs in combination with Sb has gained a great interest as such 1.0–1.15 eV material. The fabricated GaInP/GaAs/GaInAsNSb solar cells had an efficiency of 44.0% under concentration, still well below the theoretical predictions, and was limited by epitaxial growth problems which are intrinsic to quaternary and quinary materials. These problems seriously affect carrier dynamics and are likely the reason for the lack of success in achieving ultimate solar cell performance beyond the 50% barrier[7]. In this work, we show how the use of GaAsSb/GaAsN short period superlattices (SL) with type-II band alignment might solve these problems at once.

Monolithic multi-junction engineering confronts an issue of paramount importance: the different sub-cells have to maintain a very low stress level during epitaxial growth, avoiding the introduction of misfit dislocations,

[1]Institute for Systems based on Optoelectronics and Microtechnology (ISOM), Universidad Politécnica de Madrid, Avda. Complutense 30, 28040, Madrid, Spain. [2]Departamento de Ciencia de los Materiales e IM y QI, Universidad de Cádiz, 11510, Puerto Real (Cádiz), Spain. [3]IMM-Instituto de Microelectrónica de Madrid (CNM-CSIC), Isaac Newton 8, PTM, E-28760, Tres Cantos (Madrid), Spain. [4]Instituto de Energía Solar (IES), Universidad Politécnica de Madrid, Avda. Complutense 30, 28040, Madrid, Spain. Correspondence and requests for materials should be addressed to J.M.U. (email: jmulloa@isom.upm.es)

which would degrade the device performance[8, 9]. This is why strain-balancing was shown before long to be a critical issue in developing efficient solar cells involving nanostructures such as quantum wells[10, 11]. Therefore, materials lattice-matched to GaAs/Ge and with a 1.0 eV or 1.15 eV bandgap are being extensively investigated. Among them, dilute nitride semiconductor alloys, such as GaInNAs or GaAsSbN, can fulfill both requirements and be used for this purpose[12]. In these highly mismatched alloys, the addition of small amounts of N leads to a dramatic reduction of the bandgap, which is explained in the framework of the band anti-crossing (BAC) model as the result of a strong interaction between the localized N states and the conduction band of the matrix[13]. However, GaAsSbN alloys show important potential advantages over GaInNAs, because the surfactant effect of Sb atoms facilitates the two-dimensional growth of the material[14]. It also has the unique property of allowing an independent tuning of both conduction and valence band energies by controlling the N and Sb contents, respectively[15]. Besides, GaAsSbN can remain lattice-matched to GaAs if the condition $[Sb] \approx 2.8 \times [N]$ is fulfilled[16], since Sb compensates the tensile strain induced by N. The GaAsSbN alloy has already been applied to solar cell technology, both as a thick layer[17–20] and as a capping layer over InAs quantum dots[21, 22]. Nevertheless, the obtained solar cell performance is not satisfactory up to now. This is due to the fact that GaAsSbN faces important epitaxial growth problems such as alloy disorder, phase separation (because of its large miscibility gap), clustering, difficult composition control (3 group-V atoms competing for the same lattice position), or N-related point defects and localized electronic states (as in any other dilute nitride alloy)[23–25]. Therefore, even within the narrow optimum growth window, achieving a low background carrier density and a long carrier lifetime and diffusion length remains still challenging in this quaternary alloy[6, 26].

The only way to overcome these problems in the growth of the quaternary alloy is to resort to new growth approaches. In this work, we show that an effective way to obtain a (pseudo)material of extremely high crystal quality and fully stoichiometric is by splitting the quaternary into two ternaries and proceed by growing a SL structure; the spatial separation of N and Sb atoms dramatically reduces miscibility problems. The SL structures can be fabricated with type-I or type-II band alignment (electrons confined in GaAsN and holes in GaAsSb) offering additional advantages over the bulk counterparts, such as long carrier lifetimes (and, therefore, enhanced collection efficiency)[27, 28] and effective bandgap tunability through period thickness. Moreover, independent conduction and valence band edge manipulation makes it possible to reproduce nominal bandgap energies of the quaternary alloy using only half the amount of Sb and N. An overall reduction of the N content should result in an overall reduction of N-related defects in the structure and, therefore, an improved crystal quality. Other SL structures based on dilute nitrides, such as GaAsN/InAsN, GaAsN/GaAsBi and GaAsBiN/GaAs have been already proposed as suitable for photovoltaic applications and studied theoretically[29–31], while GaAsN/InGaAs SLs have already been realized[32]. However, the use of SLs might also bring a major drawback, which is carrier trapping and ultimately recombination in the SL. This would result in a lower effective mobility[33], which degrades carrier transport and results in a severe reduction of the quantum efficiency.

Our results show that this is not the case in the type-II GaAsN/GaAsSb system when the thickness of the SL period is reduced to 6 nm. For such thin stacks, strong quantum tunneling comes into play producing devices with the same quantum efficiency at zero and reverse biasing, i.e. achieving a complete carrier collection under photovoltaic conditions.

Results

Crystallinity and Interface Sharpness. In the first series of samples, different SL structures containing 18 periods with a constant period thickness of 12 nm (6 nm + 6 nm) as active layer are compared. The total thickness of the SL is 200 nm and they consist of: GaAsSb/GaAs (Sample *SL-Sb*), GaAs/GaAsN (sample *SL-N*), GaAsSbN/GaAs (sample *SL-I* with expected type-I confinement) and GaAsSb/GaAsN (sample *SL-II* with expected type-II confinement). A fifth sample with a 200 nm-thick GaAsSbN bulk layer (sample *bulk*) was grown as a reference to complete the series. A scheme of the epitaxial structure and the expected band structure of samples *SL-I* and *SL-II* are shown in Fig. 1a,b respectively (see Supplementary Fig. S1a,b,c for the sketch of rest of the samples). All the samples were grown under the same Sb and N nominal fluxes; therefore, only half the amount of N and Sb was nominally used to fabricate the SL structures as compared to the bulk, and the amount of low bandgap active material was half in these structures.

The samples were structurally analyzed by transmission electron microscopy (TEM). Dark field 002 representative images of samples *SL-I* and *SL-II* are shown in Fig. 1c,d (see Supplementary Fig. S1d,e,f for the rest of the samples). In this chemically sensitive TEM imaging mode, Sb-rich regions appear brighter whereas N-rich regions appear darker than GaAs regions. It can be observed that both samples exhibit flat growth fronts and there is no evidence of dislocations or any other sort of extended defects. A detailed analysis demonstrates that *SL-I* and *SL-II* are completely pseudomorphic, and that all layers have similar compositions along the structure. The periodicity is regular throughout the whole structure with estimated period thicknesses of 12.7 nm for *SL-I* and 12.9 nm for *SL-II*, slightly larger than the nominal value of 12 nm due to a minor increase in the growth rate. Also, the interface contrast appears more abrupt in *SL-II*, indicative of reduced Sb segregation[34].

All samples from this set were investigated by high-resolution x-ray diffraction (HR-XRD). Figure 2 shows the corresponding omega-2 theta scans around the (004) GaAs reflection. The HR-XRD spectra of the ternary SLs *SL-Sb* and *SL-N* allow estimating the Sb and N composition to be 3.25% and 1.20% in the respective layers, considering a completely pseudomorphic epitaxy as observed by TEM. These two values fulfill the lattice matching condition for GaAsSbN on GaAs, as it is evidenced by the symmetrical position of the main SL peaks with respect to the substrate peak. We also observe that the secondary peaks are considerably less intense in *SL-Sb* than in *SL-N*, meaning that the *SL-Sb* sample has worse periodicity, likely due to Sb segregation in this type of structures. Assuming that there is no Sb-N interaction during growth that could modify the composition, lattice matching is expected from the nominal growth parameters also in the rest of the samples. However, in the *SL-I* and *bulk* HR-XRD spectra, the main peak appears shifted towards the tensile region of the spectrum. This indicates that

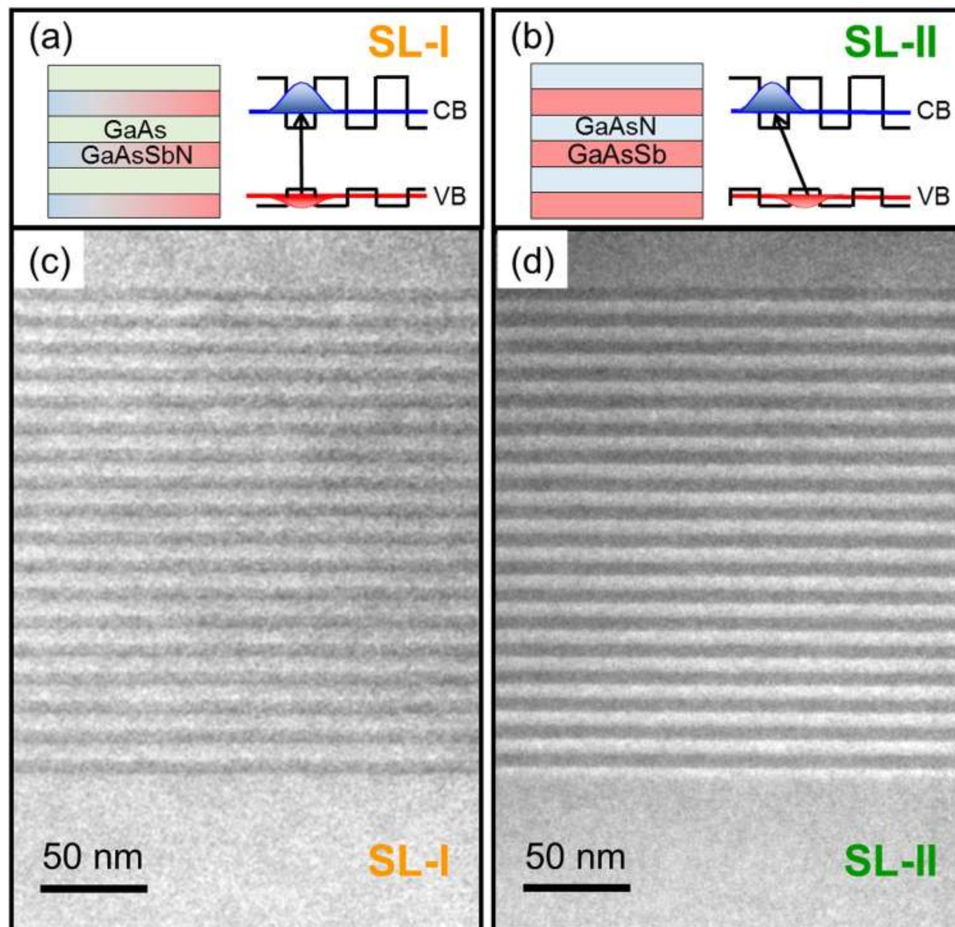

Figure 1. Epitaxial and band structure of 12 nm period SL structures. (**a**,**b**) Sketch of the epitaxial layout and expected band structure (not to scale) of samples (**a**) *SL-I* (GaAsSbN/GaAs SL) and (**b**) *SL-II* (GaAsSb/GaAsN SL). A type-I band alignment is expected in sample *SL-I*, with the maximum of the distribution probability of electron and hole wavefunctions (in blue and red, respectively) localized in the GaAsSbN layer. A type-II band alignment is expected in sample *SL-II*, with the maximum of the distribution probability of the electron and hole wavefunctions localized in the GaAsN and GaAsSb layers, respectively. (**c**,**d**) Dark field 002 TEM images of the same two samples showing the SL structure embedded in GaAs. (**c**) *SL-I*: the darker layers correspond to GaAsSbN, while the GaAs layers in the SL show the same contrast than in the buffer and capping layers. (**d**) *SL-II*: the darker layers corresponds to GaAsN whereas the brighter ones are GaAsSb.

the composition is altered from that of the ternaries due to the concomitant presence of N and Sb in the growth front. This effect is particularly strong in the bulk sample.

The main motivation in this work is to explore the alternate introduction of Sb and N atoms in the growth surface to avoid the interaction between both species. We expect that the composition in the pseudo-quaternary structure can consequently be accurately controlled. Figure 2 demonstrates that this is the case for sample *SL-II* where we find a perfectly lattice-matched spectrum implying that the expected contents were incorporated and the overall strain precisely compensated. Moreover, the narrower main peak in the SLs as compared to the bulk structure indicates a better strain and composition homogeneity, which means that clustering effects are significantly reduced in the SL structures. Remarkably, the secondary peaks are also narrower and more intense in *SL-II* as compared to *SL-I* reflecting the higher interface quality when Sb and N are incorporated separately, in agreement with what was observed by TEM.

Energy and Radiative Lifetime Tuning. The higher control over composition achievable with the type-II SL as compared to the type-I SL or the bulk is an important feature for energy tuning of the bandgap in multi-junction solar cell applications. Figure 3a shows photoluminescence (PL) spectra measured in the samples described above at 15 K. The shift of the *SL-II* emission peak energy with respect to the bandgap of GaAs (dashed vertical line) is 280 meV. This fits almost perfectly with the combined energy shifts observed for the ternary samples *SL-Sb* (27 meV) and *SL-N* (250 meV). This is a quite unique property of this system by which tuning of the valence and conduction bands, and thus the bandgap energy value, can be done setting independently the Sb and N concentrations. Such independent control is hard to reproduce in the bulk quaternary alloy. All samples were fabricated using the same nominal ternary concentrations and, yet, the sample *bulk* significantly

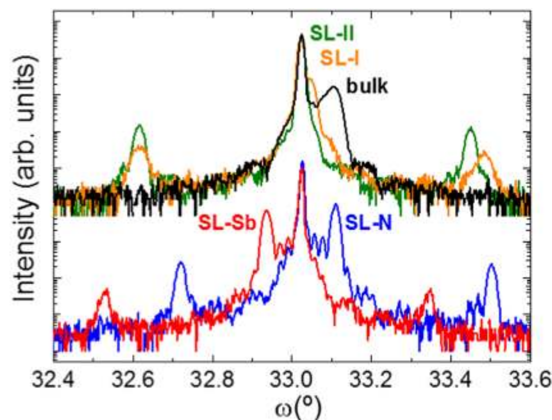

Figure 2. High resolution X-ray diffraction of the different structures. Omega-2 theta scans around the (004) GaAs Bragg reflection performed on the ternary samples *SL-Sb* and *SL-N* (below) and on the samples *SL-I*, *SL-II*, and *bulk* (above). The most intense peak at 33.0239° corresponds to GaAs. The main peak of the two ternary SLs are perfectly symmetric with respect to that of GaAs, indicating an equivalent compressive (*SL-Sb*) and tensile (*SL-N*) accumulated strain. Only the GaAsSb/GaAsN structure (*SL-II*) satisfies perfectly the lattice matching condition (main peak coincident with that of GaAs) expected from the combination of both ternaries.

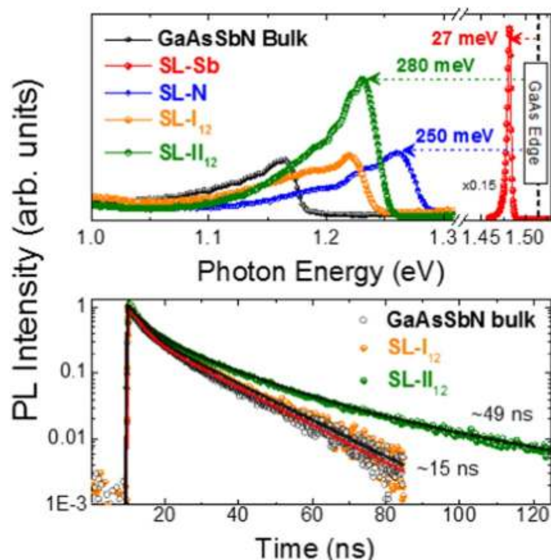

Figure 3. Photoluminescence and time-resolved photoluminescence of the different structures. (**a**) Time-integrated PL spectra of all the samples taken at low temperature (15 K) with a fixed laser power of 3 mW. The indicated energies in meV represent the energy shift of the PL peak energy of each sample with respect to the GaAs bandgap (1.46 eV). (**b**) Time-resolved PL decay curves of the samples *bulk*, *SL-I* and *SL-II*, each one measured at the energy corresponding to the PL peak taken from the spectra in (**a**). Solid lines represent the result of a multi-exponential fit to the experimental data. The (longer) radiative times obtained from this fitting are indicated in the figure. The complete deconvoluted decay time parameters are presented in Supplementary Table S1.

redshifts from the nominal bandgap value. Finite differences calculations shown below suggest that quantum confinement size effect in the 12 nm period SLs is only ~39 meV, what would only partially explain the PL peak difference of 55 meV as compared to the bulk. The redshift of the PL peak energy and the tensile position of the HR-XRD central peak shown in Fig. 2 rather points to an unwanted incorporation of N in this sample (and, to a lesser extent, also in the *SL-I* sample), which was suppressed in the *SL-II* sample using alternate deposition of the ternary compounds.

Time resolved-photoluminescence (TR-PL) decay curves measured at the PL peak energy provide further details about the carrier confinement within each sample. As shown in Fig. 3b, *SL-I* and *bulk* samples have similar decay dynamics, clearly different from those of sample *SL-II*. A multi-exponential fitting analysis is necessary to describe the decay dynamics across the full-time range and can be found as Supplementary Table S1. Yet, the larger differences occur for long times after the excitation where the decay of the luminescence of sample

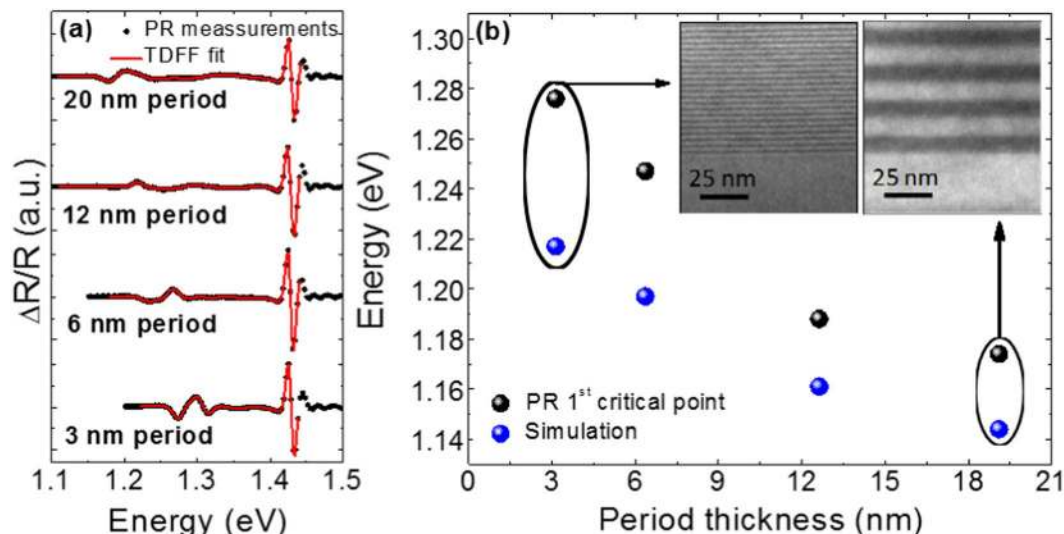

Figure 4. Photoreflectance and effective bandgap calculation as a function of period thickness. (**a**) PR spectra taken at room temperature (black dots) and TDFF fittings (red lines) for the SL structures with different periods. The minimum of the curve at lower energy corresponds to the first PR critical point, associated with the effective band gap of the sample. The effective bandgap energies obtained from PR measurements are represented by the black dots in (**b**), where also the effective bandgap energy obtained from simulations based on finite differences method are presented (blue dots). The inset in (**b**) shows dark field 002 TEM images of the samples with the thinnest and thickest period, showing an accurate control of the SL periodicity even for very thin periods of 3 nm (5 MLs GaAsSb/5 MLs GaAsN).

SL-II becomes three times slower (decay constant changes from ~15 to ~49 ns). The existence of this significantly longer radiative lifetimes at the PL peak energy for sample *SL-II* strongly supports the predominance of type-II band alignment and recombination. This is additionally supported by the calculated *SL-I*/*SL-II* ratio between the electron-hole wave function's overlap (inversely proportional to the radiative lifetime), which is ~3. Slower carrier recombination shall lead to an enhanced carrier extraction and, therefore, an improved photocurrent. Remarkably, in this sample, not only the PL band is narrower but the integrated PL emission is the most intense despite the longer carrier lifetime (see Fig. 3a)[35]. This is a clear indication of the improved crystal and interface quality produced by our method, also underlined by the fact that the PL of bulk GaAsSbN layer, despite having twice as much active material, is much weaker.

In order to investigate the formation of minibands and the effective bandgap tunability through the SL period thickness, four additional samples were grown: 200 nm-thick type-II SLs with the same N and Sb contents as the previous set of samples, but different period thickness: 3 nm, 6 nm, 12 nm and 20 nm. HR-XRD measurements indicate that all the samples are lattice-matched to GaAs and that the period thicknesses agree with the nominal values: 3.1 nm, 6.4 nm, 12.6 nm and 19.1 nm, respectively. Tuning in relevant spectral regions shall be demonstrated at room temperature. Thus, the effective bandgap energies from these SLs have been obtained from photoreflectance (PR) measurements at room temperature, shown in Fig. 4a. The PR spectra have been analyzed through the third derivative functional form (TDFF) method[36]. The lowest energy critical point obtained thereof is associated with the optical transition between electron and hole ground states. As shown in Fig. 4b, the effective bandgap energy increases rapidly as the SL period decreases, indicative of a quantum confinement size effect. The bandgap energy tuning capability saturates for periods larger than 20 nm. Noticeably, a bandgap tunability of more than 100 meV is achieved within the investigated range. These experimental values have been compared with electronic band structure calculations, performed taking into account the whole SL structure; the calculated ground state energies shown in Fig. 4b follow the same trend of the PR results, with a rigid shift to lower energies likely due to the simplified approximations assumed in the model. These findings confirm the expected quantum confinement in the structures and the ability to tune the effective bandgap at room temperature by varying the period thickness.

Single-Junction Solar Cell Performance. Efficient carrier transport through the epitaxial structure is mandatory to assess the performance of these SL structures as solar sub-cells. We have investigated the external quantum efficiency (EQE) at room temperature of five p-i-n diodes with different 750 nm-thick active regions: one GaAsSbN/GaAs type-I SL structure with 12 nm period ($SL\text{-}I_{12}$), two GaAsSb/GaAsN type-II SL structures with 12 nm ($SL\text{-}II_{12}$) and 6 nm ($SL\text{-}II_{6}$) period, a bulk GaAsSbN layer (*bulk*) and a GaAs reference sample (*GaAs*) for comparison. The Sb and N-containing samples were all grown under the same nominal fluxes. Comparing the EQE of devices based on low-dimensional structures and bulk layers with the same effective bandgap is not straightforward. On one hand, the total intrinsic region thickness should be the same to do the comparison under the same transport conditions for a given bias. On the other hand, the volume (thickness) of the absorbing material (low bandgap material) should also be the same or else the absorptance or the total light absorption would

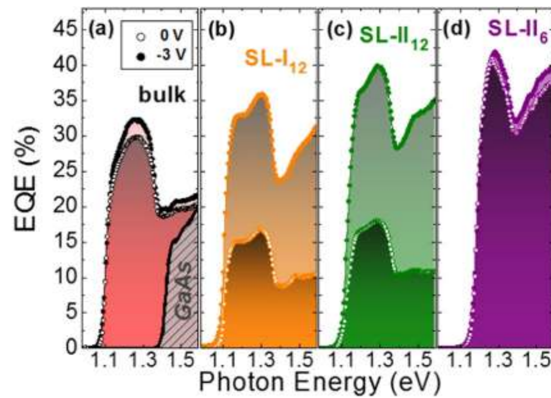

Figure 5. External quantum efficiency of the solar cell devices. EQE spectra measured at room temperature at 0 V (empty dots) and with a reverse bias voltage of −3 V (filled dots) from samples (**a**) *bulk* together with sample *GaAs* as a reference (**b**) $SL\text{-}I_{12}$ (**c**) $SL\text{-}II_{12}$ and (**d**) $SL\text{-}II_{6}$. The spectra of samples bulk and GaAs have been normalized to account for the fact that they have double amount of active material (low bandgap material).

not be directly comparable from one device to the other. Moreover, the different dimensionality of the structures will give rise to a different density of states and absorption coefficient α. Thus, to establish a fair comparison between the performance of devices of different quantity of absorbing material, we introduce an effective thickness. As the bulk sample contains twice as much Sb and N than the SLs, we can define the bulk materials as having double effective thickness with respect to the SLs, i.e. $L' = 2L$. The EQE curves for the bulk sample have been normalized as if it had the same effective thickness than the SL: $L'/2$. Such value of the EQE is calculated from the absorptance, expressed as $(1 - e^{-\alpha L})$, at half-thickness. The details of the normalization method can be found in the supplementary material. The EQE curves obtained at 0 V and −3 V are shown in Fig. 5 (see Supplementary Fig. S2 for the measured curves). I-V measurements taken under illumination indicate that the current at −3 V is already saturated in all the analyzed devices as can be seen in Supplementary Fig. S3, ensuring complete carrier collection conditions[37]. Therefore, we can define the carrier collection efficiency at 0 V as the ratio EQE(0 V)/EQE(−3 V)[37]. It can be observed that the bulk sample and the two SLs with 12 nm period provide significant conversion efficiencies in the technologically relevant 1.15 eV spectral region.

Figure 5a shows that there is no difference between the 0 V and −3 V curves for the GaAs device, indicating 100% carrier collection efficiency at 0 V, as expected. Nevertheless, there is a small enhancement of the EQE from 0 to −3 V in the GaAsSbN device, which shows a peak carrier collection efficiency around 95%. The reduced carrier collection efficiency in the GaAsSbN structure is likely an indication of non-radiative recombination at point defects or carrier localization in potential minima induced by strain and composition modulation in the quaternary alloy[38,39]. Moreover, for energies slightly above the bandgap, the EQE is larger in the GaAsSbN bulk layer than in the GaAs reference (both with the same thickness). This enhancement shall be attributed to the increase of the joint density of states, reported for dilute nitrides, arising from a larger electron effective mass and thus a better matching to the hole band dispersion[40–42].

Regarding the 12 nm period SLs, both the normalized and raw EQE are larger in the $SL\text{-}II_{12}$ sample than in $SL\text{-}I_{12}$ as shown in Fig. 5b,c (and Supplementary Fig. S2b,c), in analogy to the PL emission intensity. This exemplifies the benefits of type-II SLs which, thanks to an improved crystal and interface quality and, in this case, also longer carrier lifetimes, show enhanced optical and transport properties. Yet, the EQE of the $SL\text{-}II_{12}$ and $SL\text{-}I_{12}$ devices also exemplifies the potential drawback of a non-optimized SL structure suffering from slow carrier extraction dynamics. In both samples, EQE increases with the reverse bias limiting severely its application in solar cells. In this case, the carrier extraction at 0 V is not efficient enough because the weak electronic coupling for a 12 nm period prevents carrier tunneling through the SL barriers in the presence of the built-in electric field. However, it can be easily restored by reducing the period from 12 to 6 nm as shown in Fig. 5d. The fully optimized SL structure ($SL\text{-}II_{6}$) shows a normalized EQE which not only is the largest of all samples, but is virtually the same at 0 V as at −3 V. This means improved carrier collection at 0 V and a large overlap of the SL minibands across the structure. A quantum treatment of the transport along the SL[43] is out of the scope of this work but, as a first approximation, we have calculated the transmission coefficient based on analytic expressions using the transfer matrix approach[44]. In such framework, the electronic transmission through a finite array of barriers represents the ability of a confined electron to be transmitted through the periodic structure. Figure 6 shows the transmission coefficient for electrons below the GaAs bandgap energy as a function of the period thickness (corresponding transmission coefficient for holes are shown in Supplementary Fig. S4). The results clearly show that electronic coupling and tunneling is strongly enhanced reducing the period from 12 to 6 nm. As a figure of merit, the transmission window halfwidth around the ground state energy increases from 0.3 meV to 21 meV in halving the SL period. We conclude that the reduction of the period thickness from 12 to 6 nm leads to a strong wavefunction overlap and electronic coupling that solve the minority carrier extraction problem without impairing the already mentioned benefits of type-II GaAsSb/GaAsN SL. Although we do not solve the quantum transport equations, our experimental results and calculations for the optimized $SL\text{-}II_{6}$ sample strongly suggest that vertical transport

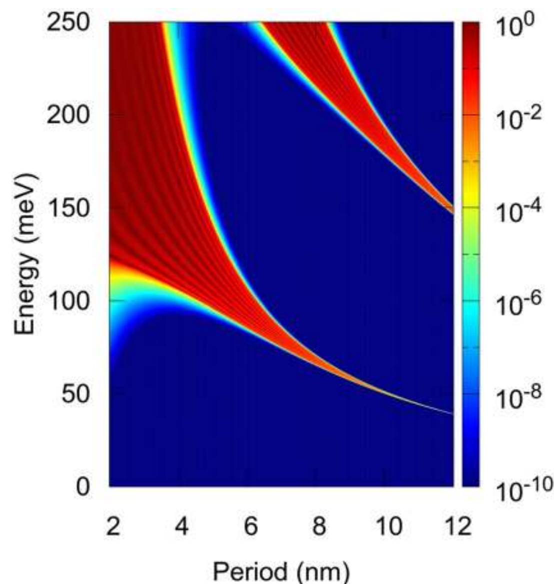

Figure 6. Transmission coefficient for electrons below the GaAs bandgap energy as a function of the period thickness. Contour plot of the electron transmission coefficient for a 12 barrier/quantum well array as a function of period thickness between 2 and 12 nm. The height of the barrier is 250 meV and the effective mass 0.146 m_0, which are the parameters used to model the *SL-II* sample in Fig. 4b. The color bar is in log scale. The formation of electronically coupled minibands for small periods becomes evident by the broadening of the high transmission coefficient region.

is more efficient than radiative and non-radiative recombination under photovoltaic conditions, though the situation at the operating voltage of the solar cell (positive voltage) could be different and still has to be analyzed.

Overall, Fig. 5 shows that the peak EQE is 30% higher in the thin period SL structure than in the GaAsSbN bulk sample. In this SL sample, the difference in the measured EQE between −3 and 0 V is also smaller than in the bulk. The estimated carrier collection efficiencies at 0 V are 100% vs. 93% (peak values), respectively. Carrier transport is therefore improved as compared to the bulk and complete carrier collection at 0 V is achieved. This is likely due to the suppression of non-radiative recombination and/or carrier localization effects due to composition and strain inhomogeneities, in agreement with the outcomes of the PL and XRD analysis. This improvement in carrier transport is, however, not enough to explain the 30% enhancement in the peak EQE. A larger absorption coefficient in the SL structure is therefore inferred, strongly contributing to the observed EQE improvement. This is a very promising result, since it could in principle guarantee current matching in GaAs/1.0 eV/Ge solar cells. Indeed, these results suggest that using strain-balanced GaAsSb/GaAsN type-II SLs with thin periods should be a better alternative to thick GaAsSbN layers in this type of solar cells.

Discussion

Strain-balanced GaAsSb/GaAsN SLs grown on GaAs are shown to overcome the unavoidable growth problems related to the quaternary GaAsSbN alloy that affect both thick layers and GaAsSbN/GaAs SLs. The spatial separation of N and Sb atoms gives rise to a superior composition and effective bandgap control, as well as to an improved crystal quality and interface abruptness. Moreover, the new structures allow additional tuning of the effective bandgap through the period thickness due to quantum confinement. The type-II band alignment results in long radiative lifetimes that are beneficial for carrier extraction. Remarkably, despite the long carrier lifetimes, the new structures show a strongly enhanced luminescence compared to thicker quaternary bulk layers having twice as much active material. A significant EQE at 1.15 eV is demonstrated, as well as efficient carrier transport by tunneling though the SL minibands for period thicknesses of ~6 nm. For these thin periods, a strong net enhancement of EQE over equivalent bulk counterparts is demonstrated under photovoltaic conditions. In this SL with the optimum design, however, the absorption edge is 50–100 meV over the target value due to the effect of quantum confinement, so the N and Sb contents should be slightly increased to compensate for that. All these characteristics make short period GaAsSb/GaAsN SLs the ideal (pseudo)material candidate to be monolithically series-connected in ultimately efficient GaAs/Ge-based multi-junction solar cells.

Methods

Growth details. The analyzed samples were all grown by solid source molecular beam epitaxy in a Riber 32 system using GaAs (001) n^+ substrates under As_4 overpressure conditions. Each sample consists of a 250 nm-thick n-doped GaAs buffer layer, a 200 nm or 750 nm-thick undoped active layer grown at 470 °C at a growth rate of 1 ML/s, and a 50 nm-thick p-doped GaAs layer deposited on top. The device configuration is therefore a p-i-n junction. The nominal n and p-type doping concentration was $2 \cdot 10^{18}\ cm^{-3}$. The Sb flux was supplied from a Knudsen effusion cell whereas the atomic N flux came from a radio-frequency plasma source using a 0.1 sccm

flow of pure N_2. The growth was *in-situ* monitored by reflective high energy electron diffraction (RHEED) which allowed the verification of a two-dimensional growth mode throughout the whole structure.

Materials characterization. TEM was used to obtain dark field 002 images, which were acquired in a JEOL 2100 microscope operating at 200 keV. HR-XRD rocking-curve scans using the Cu-Kα1 line (1.54056 Å) were performed with an X'Pert Pro Pan'alytical commercial system. Low temperature (15 K) PL measurements were carried out using a He-Ne laser with a power of 3 mW. The emitted light was dispersed through a 1 m-spectrometer and detected using a liquid-nitrogen cooled Ge-detector and standard lock-in techniques. TR-PL experiments were performed at low temperature exciting the sample with 405 nm pulsed laser light. Decay curves were recorded by a time correlated single photon counting system based on a fast-infrared photomultiplier attached to a 0.3 m-focal length spectrometer. The average excitation power density was 0.6 W/cm^2 at 10 MHz. Multi-exponential deconvolution analysis was done taking into account the system response measured with a 980 nm ps laser. Time resolution after system response deconvolution is ~200 ps. The optical analysis was completed with PR measurements. PR was performed at room temperature using the 325 nm line of a 15 mW He-Cd laser as pump beam (chopped at 777 Hz), the monochromatic (1/8 m-spectrometer) probe beam from a 150 W QTH lamp, and a cooled InGaAs-photodetector.

Electronic band structure calculation. The calculation is based on finite differences methods. Single band effective mass approximation was used with input parameters for the Sb and N contents obtained from the HR-XRD spectra of the ternary samples, and the period thickness estimated from the TEM measurements of each sample. The bandgap energy and band offsets of GaAsN were obtained considering the BAC predictions in first order perturbation theory[13], with the specific values for the electron effective mass and BAC parameters described elsewhere[45]. Regarding the GaAsSb layers, their bandgap energy and band offsets were estimated using experimental results for GaAsSb pseudomorphically grown on GaAs[46]. The hole effective mass was obtained from a linear interpolation between the binaries.

Device fabrication. The thickest samples (750 nm active layer) were processed in 200 µm-diameter mesa-etched devices using standard fabrication techniques. The mesa structures were defined by wet etching using a H_3PO_4-H_2O_2-H_2O (1:1:8) solution. The p-type contact, deposited on top of the mesa, was Au/Au-Zn/Au (100/800/2000 Å). A common n-type contact consisting on Au-Ge/Au (800/2000 Å) was evaporated on the substrate side. The contacts were exposed to an annealing process at 400 °C during 1 minute.

Device characterization. Photocurrent measurements were carried out using light from a QTH lamp which was dispersed through a 0.34 m monochromator and directed through the optical path to the sample. A K230 Keithley sourcemeter as well as a K617 Keithley electrometer were employed. To obtain the EQE, the photocurrent data was first converted into responsivity dividing by the power per unit area of the QTH lamp (measured using a calibrated Si photodiode and a pyroelectric photodetector) multiplied by the diode top metal-free area. Finally, responsivity was converted to EQE multiplying by the photon energy divided by the electron charge.

Transmission coefficients calculation. The parameters used in the calculation for the bandgap energies, effective masses and band offsets are those used in the electronic band structure calculations. Calculations were done separately for electrons and holes transmitted through 12 consecutive barriers at flat band condition.

Data availability. All data generated or analyzed during this study are included in this published article (and its Supplementary Information files).

References

1. Green, M. A. *et al*. Solar cell efficiency tables (version 49). *Prog. Photovoltaics Res. Appl.* **25**, 3–13 (2017).
2. Kurtz, S. R., Myers, D. & Olson, J. M. Projected performance of three- and four-junction devices using GaAs and GaInP. *Conf. Rec. IEE Photovoltaic Spec. Conf.* **26**, 875–878 (1997).
3. Toprasertpong, K. *et al*. Absorption threshold extended to 1.15 eV using InGaAs/GaAsP quantum wells for over-50%-efficient lattice-matched quad-junction solar cells. *Prog. Photovoltaics Res. Appl.* **24**, 533–542 (2016).
4. Tanabe, K. A review of ultrahigh efficiency III–V semiconductor compound solar cells: multijunction tandem, lower dimensional, photonic up/down conversion and plasmonic nanometallic structures. *Energies* **2**, 504–530 (2009).
5. Derkacs, D., Jones-Albertus, R., Suarez, F. & Fidaner, O. Lattice-matched multijunction solar cells employing a 1 eV GaInNAsSb bottom cell. *J. Photonics Energy* **2**, 021805–8 (2012).
6. Jackrel, D. B. *et al*. Dilute nitride GaInNAs and GaInNAsSb solar cells by molecular beam epitaxy. *J. Appl. Phys.* **101**, 114916–8 (2007).
7. Friedman, D. J. & Kurtz, S. R. Breakeven criteria for the GaInNAs junction in GaInP/GaAs/GaInNAs/Ge four-junction solar cells. *Prog. Photovoltaics Res. Appl.* **10**, 331–344 (2002).
8. Yamaguchi, M. III–V compound multi-junction solar cells: present and future. *Sol. Energy Mater. Sol. Cells* **75**, 261–269 (2003).
9. Friedman, D. J. Progress and challenges for next-generation high-efficiency multijunction solar cells. *Curr. Opin. Solid State Mater. Sci.* **14**, 131–138 (2010).
10. Griffin, P. R. *et al*. Effect of strain relaxation on forward bias dark currents in GaAs/InGaAs multiquantum well p-i-n diodes. *J. Appl. Phys.* **80**, 5815–5820 (1996).
11. Ekins-Daukes, N. J. *et al*. Strain-balanced GaAsP/InGaAs quantum well solar cells. *Appl. Phys. Lett.* **75**, 4195–4197 (1999).
12. Sabnis, V., Yuen, H. & Wiemer, M. High-efficiency multijunction solar cells employing dilute nitrides. *AIP Conf. Proc.* **1477**, 14–19 (2012).
13. Shan, W. *et al*. Band anticrossing in GaInNAs alloys. *Phys. Rev. Lett.* **82**, 1221–1224 (1999).
14. Cheah, W. K. *et al*. Surfactant and impurity properties of antimony on GaAs and $GaAs_{1-x}N_x$ on GaAs [100] by solid source molecular beam epitaxy. *Thin Solid Films* **488**, 56–61 (2005).
15. Lin, Y. T., Ma, T. C., Chen, T. Y. & Lin, H. H. Energy gap reduction in dilute nitride GaAsSbN. *Appl. Phys. Lett.* **93**, 171914–3 (2008).

16. Wicaksono, S., Yoon, S. F., Tan, K. H. & Cheah, W. K. Concomitant incorporation of antimony and nitrogen in GaAsSbN lattice-matched to GaAs. *J. Cryst. Growth.* **274**, 355–361 (2005).
17. Tan, K. H. *et al.* Molecular beam epitaxy grown GaNAsSb 1 eV photovoltaic cell. *J. Cryst. Growth* **335**, 66–69 (2011).
18. Ahsan, N. *et al.* Effect of Sb on GaNAs intermediate band solar cells. *IEEE J. Photovoltaics* **3**, 730–736 (2013).
19. Tan, K. H. *et al.* Study of a 1 eV GaNAsSb photovoltaic cell grown on a silicon substrate. *Appl. Phys. Lett.* **104**, 103906–4 (2014).
20. Kim, T. W. *et al.* 1.25-eV GaAsSbN/Ge double-junction solar cell grown by metalorganic vapor phase epitaxy for high efficiency multijunction solar cell application. *IEEE J. Photovoltaics* **4**, 981–985 (2014).
21. Utrilla, A. D. *et al.* GaAsSb/GaAsN short-period superlattices as a capping layer for improved InAs quantum dot-based optoelectronics. *Appl. Phys. Lett.* **105**, 043105–4 (2014).
22. Utrilla, A. D. *et al.* Impact of alloyed capping layers on the performance of InAs quantum dot solar cells. *Sol. Energy Mater. Sol. Cells* **144**, 128–135 (2016).
23. Harmand, J. C. *et al.* GaNAsSb: how does it compare with other dilute III–V-nitride alloys? *Semicond. Sci. Technol.* **17**, 778–784 (2002).
24. Buyanova, I. A., Chen, W. M. & Tu, C. W. Magneto-optical and light-emission properties of III–As–N semiconductors. *Semicond. Sci. Technol.* **17**, 815–822 (2002).
25. Chauveau, J. M. A. *et al.* Correlations between structural and optical properties of GaInNAs quantum wells grown by MBE. *J. Cryst. Growth* **251**, 383–387 (2003).
26. Miyashita, N., Ahsan, N. & Okada, Y. Generation and collection of photocarriers in dilute nitride GaInNAsSb solar cells. *Prog. Photovoltaics Res. Appl.* **24**, 28–37 (2016).
27. Razeghi, M. *et al.* Recent advances in LWIR type-II InAs/GaSb superlattice photodetectors and focal plane arrays at the center for quantum devices. *Proc. IEEE* **97**, 1056–1066 (2009).
28. Fujita, H. *et al.* Open-circuit voltage recovery in type II GaSb/GaAs quantum ring solar cells under high concentration. *Prog. Photovoltaics Res. Appl.* **23**, 1896–1900 (2015).
29. Bhusal, L. & Freundlich, A. GaAsN/InAsN superlattice based multijunction thermophotovoltaic devices. *J. Appl. Phys.* **102**, 074907–5 (2007).
30. Hwang, J. & Phillips, J. D. Band structure of strain-balanced GaAsBi/GaAsN superlattices on GaAs. *Phys. Rev. B* **83**, 195327–7 (2011).
31. Alemu, A. & Freundlich, A. Dilute nitride-based III–V heterostructures for unhindered carrier transport in quantum-confined p-i-n solar cells. *Proc. of SPIE.* **7211**, 72110M–4 (2009).
32. Wu, P. H. *et al.* Strain-compensated GaAsN/InGaAs superlattice structure solar cells. *Jpn. J. Appl. Phys.* **45**, L647–L649 (2006).
33. Toprasertpong, K. *et al.* Microscopic observation of carrier-transport dynamics in quantum-structure solar cells using a time-of-flight technique. *Appl. Phys. Lett.* **107**, 043901–5 (2015).
34. Sanchez, A. M. *et al.* Blocking of indium incorporation by antimony in III-V-Sb nanostructures. *Nanotechnology* **21**, 145606–8 (2010).
35. Ulloa, J. M. *et al.* High efficient luminescence in type-II GaAsSb-capped InAs quantum dots upon annealing. *Appl. Phys. Lett.* **101**, 253112–5 (2012).
36. Aspnes, D. E. Third-derivative modulation spectroscopy with low-field electroreflectance. *Surf. Sci.* **37**, 418–442 (1973).
37. Fujii, H., Wang, Y., Watanabe, K., Sugiyama, M. & Nakano, Y. High-aspect ratio structures for efficient light absorption and carrier transport in InGaAs/GaAsP multiple quantum-well solar cells. *IEEE J. Photovoltaics* **3**, 859–867 (2013).
38. Hubin, J. & Shah, A. V. Effect of the recombination function on the collection in a p-i-n solar cell. *Philos. Mag. B* **72**, 589–599 (1995).
39. Feng, S. W., Lai, C. M., Chen, C. H., Sun, W. C. & Tu, L. W. Theoretical simulations of the effects of the indium content, thickness, and defect density of the i-layer on the performance of p-i-n InGaN single homojunction solar cells. *J. Appl. Phys.* **108**, 093118–7 (2010).
40. Bhusal, L. & Freundlich, A. Band structure and absorption properties of $GaAs_{1-x}$ N_x/$InAs_{1-y}N_y$ short period superlattices strained to InP (001). *Phys. Rev. B* **75**, 075321–12 (2007).
41. Turcotte, S. *et al.* Experimental investigation of the variation of the absorption coefficient with nitrogen content in GaAsN and GaInAsN grown on GaAs (001). *J. Appl. Phys.* **104**, 083511–5 (2008).
42. Tomić, S. *et al.* Influence of conduction-band nonparabolicity on electron confinement and effective mass in GaN_xAs_{1-x}/GaAs quantum wells. *Phys. Rev. B* **69**, 245305–12 (2004).
43. Aeberhard, U. Simulation of nanostructure-based high-efficiency solar cells: challenges, existing approaches, and future directions. *IEEE J. Sel. Topics Quantum Electron.* **19**, 4000411–11 (2013).
44. Sprung, D. W. L., Wu, H. & Martorell, J. Scattering by a finite periodic potential. *Am. J. Phys.* **61**, 1118–1124 (1993).
45. Ulloa, J. M., Sánchez-Rojas, J. L., Hierro, A., Tijero, J. M. G. & Tournié, E. Effect of nitrogen on the band structure and material gain of In_yGa_{1-y} $As_{1-x}N_x$ – GaAs quantum wells. *IEEE J. Sel. Topics Quantum Electron.* **9**, 716–722 (2003).
46. Teissier, R. *et al.* Temperature-dependent valence band offset and band-gap energies of pseudomorphic GaAsSb on GaAs. *J. Appl. Phys.* **89**, 5473–5477 (2001).

Acknowledgements

We acknowledge funding from the Spanish MINECO through projects MAT2013-47102-C2-2-R and MAT2016-77491-C2-1-R, TEC2015-64189-C3-2-R and Grant AIC-B_2011-0806, and from CSIC through project 2015-50-I021. DFM acknowledges financial support of Comunidad de Madrid (S2013/MAE-2780). We would also like to thank Maika Sabido (ISOM-UPM) for help with processing of the samples.

Author Contributions

A.G. and A.D.U. did the MBE growth of the samples, the XRD and PL characterization, the device processing and the IV and E.Q.E. measurements. D.F.R., V.B., T.B. and D.G. performed the TEM measurements and analysis. J.M.L. did the calculations of the transmission coefficient. D.F.M. did the PR measurements and analysis. B.A. performed the TR-PL measurements and analysis. A. Guzman performed the finite differences calculations. A.H. mounted the IV and PC measurement set-up and helped with device characterization. J.M.U. conceived, designed and supervised the research. All the authors discussed the results and commented on the manuscript.

Additional Information

Supplementary information accompanies this paper at doi:10.1038/s41598-017-04321-4

Competing Interests: The authors declare that they have no competing interests.

Publisher's note: Springer Nature remains neutral with regard to jurisdictional claims in published maps and institutional affiliations.

Open Access This article is licensed under a Creative Commons Attribution 4.0 International License, which permits use, sharing, adaptation, distribution and reproduction in any medium or format, as long as you give appropriate credit to the original author(s) and the source, provide a link to the Creative Commons license, and indicate if changes were made. The images or other third party material in this article are included in the article's Creative Commons license, unless indicated otherwise in a credit line to the material. If material is not included in the article's Creative Commons license and your intended use is not permitted by statutory regulation or exceeds the permitted use, you will need to obtain permission directly from the copyright holder. To view a copy of this license, visit http://creativecommons.org/licenses/by/4.0/.

© The Author(s) 2017